Measurement and modeling of the radio frequency sheath impedance in a large magnetized plasma

J. R. Myra,[1] C. Lau,[2] B. Van Compernolle,[3,4] S. Vincena[3] and J. Wright[5]

[1]*Lodestar Research Corporation, Boulder, Colorado 80301, USA*
[2]*Oak Ridge National Laboratory, Oak Ridge, Tennessee 37831, USA*
[3] *Department of Physics and Astronomy, University of California, Los Angeles, California 90095, USA*
[4]*Present affiliation: General Atomics, San Diego, California 92186, USA*
[5]*MIT Plasma Science and Fusion Center, Cambridge, Massachusetts 02139, USA*

April 2020
(revised June 2020)

submitted to
Physics of Plasmas

ORNL/4000158507-5; DOE-ER/54392-96 LRC-20-183

LODESTAR RESEARCH CORPORATION
2400 Central Avenue
Boulder, Colorado 80301

Measurement and modeling of the radio frequency sheath impedance in a large magnetized plasma

J. R. Myra,[1,a)] C. Lau,[2] B. Van Compernolle,[3,4] S. Vincena[3] and J. Wright[5]

[1]*Lodestar Research Corporation, Boulder, Colorado 80301, USA*
[2]*Oak Ridge National Laboratory, Oak Ridge, Tennessee 37831, USA*
[3] *Department of Physics and Astronomy, University of California, Los Angeles, California 90095, USA*
[4]*Present affiliation: General Atomics, San Diego, California 92186, USA*
[5]*MIT Plasma Science and Fusion Center, Cambridge, Massachusetts 02139, USA*

Abstract

The DC and RF properties of radio frequency (RF) driven sheaths were studied in the Large Plasma Device (LAPD) at the University of California, Los Angeles. The experiments diagnosed RF sheaths on field lines connected to a grounded plate at one end and an ion cyclotron range of frequencies (ICRF) antenna at the other end. The experimental setup permitted measurement of the RF sheath impedance at the plate as a function of DC sheath voltage, with the latter controlled by varying the RF current applied to the antenna. The DC current-voltage characteristics of these sheaths and the RF sheath impedance measurements were compared with modeling. Hot electrons, present in the LAPD plasma, were inferred to contribute significantly to both the DC and RF currents and hence the RF impedance. It was postulated that at very low power hot electrons could not access the region of the plasma subject to RF waves, resulting in an increased RF impedance. Within some experimental limitations and significant assumptions, an RF sheath impedance model was verified by the experimental data.

Keywords: radio-frequency, sheath, impedance, rectification, ICRF, LAPD

a) Author to whom correspondence should be addressed: jrmya@lodestar.com

I. Introduction

Magnetized plasma sheaths occur when magnetically confined plasmas come into contact with material surfaces, thus they are of great importance for fusion devices such as tokamaks and stellarators. Static magnetized sheaths have been the subject of numerous studies.[1-4] Dynamic sheaths also form near the material-plasma interface when radio-frequency (RF) fields are present.[5,6] RF sheaths are of particular interest for fusion-relevant plasmas when the RF fields are in the ion cyclotron range of frequencies (ICRF). While ICRF waves show great promise for economical plasma heating, current drive and other applications, they also tend to interact strongly with the boundary plasma in some situations. The electrostatic potentials V_{rf} that characterize a strong ICRF sheath in fusion devices is many times larger than the ~ $3T_e$ static thermal sheath in deuterium plasmas, where T_e is the electron temperature at the sheath entrance. The oscillating RF potential is rectified to produce a DC sheath potential of similar magnitude in order to confine most of the electrons at all phases of the RF cycle.[5,7] Thus ions are strongly accelerated through the sheath into the surface. The resulting boundary interactions are typically deleterious to performance, giving rise to enhanced ion sputtering, impurity release and enhanced RF power deposition on the affected surfaces.[8-13] Indeed many experiments on fusion devices have reported similar and related findings.[13-21]

Given the potential impact of ICRF sheaths on fusion experiments, much effort has been devoted to modeling and prediction of RF sheath properties.[22-29] In this regard it is useful to distinguish several different types of RF sheaths. Particularly relevant to the antenna surface itself and nearby limiter surfaces are so-called magnetically connected sheaths. In this case the surface either directly acts as the source of the RF potential driving the sheath or the surface is connected by a magnetic field line to the RF source. Examples of such studies include the work described in Refs. 5, 17, 23 and 30-33. A second case arises when the surface in question has no direct magnetic connection to the source, e.g. the antenna, but instead the surface in question is impacted by propagating waves, either the ICRF fast wave, or the slow wave.[20,26,27,30,34]

The spatial scale of an RF sheath, like its static counterpart, is the larger of several Debye lengths and the ion sound radius or gyro-radius. The width of the Debye, i.e. non-neutral, portion of the sheath increases with the DC bias potential and amplitude of the RF waves. However, the spatial scale of the sheath is always small compared with global scale lengths in high density plasmas and is usually modeled as a boundary condition (BC). This sheath BC provides, among other things, an effective surface sheath impedance[28,35-37] for the upstream RF fields, where upstream refers to the plasma at the sheath entrance. RF sheath impedance models in both nonlinear fluid[38,39] and particle-in-cell (PIC) models have been developed in several frameworks[40,41] and compared.[42,43]

In this paper our goal is to report on experimental measurements of the RF sheath impedance made on the Large Plasma Device (LAPD)[44] and to compare those measurements with an RF sheath impedance model. The particular experimental setup, described in detail in Sec. II, facilitates RF impedance measurements on a grounded tungsten plate immersed in the tenuous edge plasma of LAPD, where the plate is magnetically connected to an ICRF antenna. It is shown that RF antenna sheaths DC bias the field lines connected to the plate. At the same time, RF fields impact the plate and create RF potential oscillations, and RF currents between the plate and ground which are directly measurable and in fact time-resolved over the RF phase. This setup thus enables an RF impedance measurement as a function of RF antenna voltage, where the latter controls both the RF wave amplitude at the plate and the DC bias of the field lines.

In LAPD, the plasma is created by an emissive cathode source.[44] This leads to the presence of a relatively hot, but tenuous, population of electrons in addition to the bulk cold background population in the edge plasma. DC currents, modified during RF operation, also flow between various surfaces on LAPD including the tungsten plate. Both the presence of a tail electron population and DC current flow in the plasma and vessel walls are likely to be realistic features of tokamak scrape-off layer (SOL) plasmas as well. Indeed DC currents during ICRF operation have been reported in several experiments[45-47] and models for DC current flow have been investigated.[22,48,49] In the LAPD experiments described here, the existence of a DC bias not directly created by the RF fields at the tungsten plate is associated with DC current flow through the plasma and completed at the plate and in the vessel walls. Both the electron tail population and the "independent" DC bias require a generalization of the sheath impedance models described in Refs. 38 and 39. That generalization is also described in the present paper.

In addition to the work cited in the preceding paragraphs, there have been a number of other studies that are closely related to the topics under consideration here. The sheath and bulk plasma potential properties from the emissive cathode in LAPD were studied in Ref. 50. RF sheaths and associated convective cells in LAPD have been reported[33] with follow up work on the mitigation effect of insulating antenna sidewalls.[51] In other devices, RF electric field measurements near launchers have been performed using a spectroscopic technique.[52] Internal sheath electric fields were examined[53] in the IShTAR device[54] and slow wave driven sheaths in that device were modeled.[55] RF sheaths have also been studied in the ALINE device.[56] In a separate class of works, the effect of fast electrons on static sheath potentials and sheath structure were studied theoretically[57,58] The work was later extended to RF sheaths.[59]

It is well known that DC rectification of RF sheath potential leads to RF-driven convection,[60,61] an effect that has been recently modeled for the ASDEX-U antenna.[62] The DC voltage is also, as mentioned previously, closely connected to both parallel and cross-field current

flow in the plasma to the vessel walls. Cross-field current is expected to be governed in part by turbulent conductivity.[63]

Finally, RF sheaths in experimental fusion-related devices share some physical similarities with the RF sheaths encountered in plasma processing devices, although the parameter regimes, magnetic field configuration and geometry can be somewhat different. There is a vast literature on RF plasma processing sheaths; a summary is beyond the scope of the present introduction, but a few sample citations are given in Refs. 64-66.

The plan of our paper is as follows. In Sec. II the details of the LAPD experimental setup relevant to our study are presented along with an overview of the diagnostics. In Sec. III we review the theoretical model for analyzing the data. Experimental results and model comparisons are given in Sec. IV. Finally, Sec. V presents further discussion and our conclusions.

II. Experimental setup and diagnostics

LAPD is a linear plasma device, with a cylindrical vacuum vessel approximately 30 m in length and 1 m in diameter. It typically operates with an axial magnetic field in the range of 0.5 – 2.0 kG, a central plasma density n_e up to 10^{13} cm^{-3}, bulk central electron temperature T_e up to 10 eV and cold ions. LAPD operates at a 1 Hz pulse rate, with plasma discharge pulse lengths on the order of 10 ms. The experiments described in this paper were carried out in a singly ionized ^{4}He plasma at B = 1 kG.

The LAPD plasma used for the present experiments is created by a large BaO emissive cathode and a smaller LaB_6 emissive cathode on opposite sides of LAPD, the latter providing a high-density central plasma column. The emissive cathodes create a small population of ~ 50 eV electrons which collisionally ionize the working gas and sustain the plasma. These hot electrons will be seen to play an important role in the interpretation of the measurements.

LAPD is equipped with an RF antenna operating at 2.5 MHz with a maximum RF power of ~ 100 kW. The antenna used here is a single strap antenna with a current strap 6 cm wide, inside a 10 cm wide box.[33] In this experiment it operated without a Faraday screen. The RF frequency and magnetic field put the ICRF waves in the high harmonic regime at $\omega/\Omega_i = 6.3$. For the geometry of the sheath experiments described in this paper, the magnetic field does not play a significant role since it is directed parallel to the surface normal of the tungsten plate under consideration.

LAPD diagnostics relevant to the present study include a computer-controlled probe, movable in all three dimensions, which can be operated as either a Langmuir probe for measuring the characteristics of the target plasma or as an emissive probe for measuring both the DC and time-resolved RF plasma potentials. The time response of the emissive probe in this experiment is

determined by the distributed capacitance in the copper wires contained in the probe shaft and by the connection impedance between the probe tip and the plasma. The emissive probe was determined to be able to effectively capture plasma potential oscillations up to 10 MHz by connecting the probe tip to the output of a signal generator through a resistor approximating the sheath. More details on the emissive probe response may be found in Ref. 67.

The potential of the emissive probe was measured with respect to the machine wall potential with an isolating, high-impedance (10 MOhm) differential probe (Tektronix P5200A) which has large common-mode rejection. The probe shaft was RF grounded to the machine wall by connecting approximately coaxial copper braids across any insulating joints, with a number of parallel capacitors (also arranged coaxially) for DC isolation. The signals on the probe are an order of magnitude smaller when the probe is in a region of low RF power, or when the probe is retracted out of the plasma, compared to when the probe is in the region of interest for the experiment, providing confidence that ground loops or stray pick-up are not an issue.

A grounded tungsten plate measuring 10 cm × 10 cm inserted into the edge plasma was equipped with a Pearson current probe for measuring the DC and time-resolved RF current flowing from the plate to ground.

LAPD has probe access every 32 cm along the axial direction. Typically, a probe moves through a series of user defined positions. At each position, data from several plasma pulses is acquired and stored, before moving to the next position. Since the LAPD plasma is highly reproducible, an ensemble measurement of the plasma parameters can thus be obtained. The LAPD coordinate system has the z-direction along the axis of the device, pointing towards the BaO cathode. The origin z = 0 is taken as the axial position of the antenna. The (x,y) coordinates are centered on the center of the cylindrical device. More details of the LAPD experiment and its diagnostics and control systems are given in Ref. 44.

The setup and geometry for our experiments are illustrated in Figs. 1 and 2. Figure 1 shows a top view. The antenna was inserted radially into LAPD and positioned at the edge of the high-density core plasma. Limiter plates were positioned on either side of the antenna to prevent a direct connection along field lines between the antenna and the cathode/anode on either end of the device. The region of most interest for this paper is between the limiter plate at port 19 and the ICRF antenna at port 30. The tungsten plate at port 24 is normal to the magnetic field lines (i.e. the unit normal to the surface is parallel to the axial magnetic field B) and magnetically connected to the RF antenna by the magnetic field. The movable emissive probe was installed at port 24 to measure the plasma potential on these field lines and was oriented so as to avoid shadowing the tungsten plate as much as possible. The distance between the emissive probe and tungsten plate was as close as possible, a few cm. The SOL region in question was mostly, but not entirely shadowed from the BaO cathode source at port 0 by the limiter plate.

A schematic of the cross-sectional geometry is shown in Fig. 2. Notable in this figure is a DC voltage "hot spot" denoted by a large red dot. As shown in Sec. IV, the voltage at this hot spot scales linearly with the antenna RF voltage and is roughly the maximum DC voltage on field lines connected to the tungsten plate surface. Most of the measurements reported on in this paper were taken at the location of the hot spot. The results of a vertical scan, indicated by the red line in Fig. 2 will also be discussed. Target plasma measurements using the Langmuir probe were taken along the dotted green line shown in this figure.

The main results of the paper were obtained from an RF antenna current scan that resulted in modified RF and DC currents from the plate to ground, and modified RF and DC voltages on the field line at the hot spot. These measurements enabled a determination of the RF impedance of the sheath on the tungsten plate for varying conditions of DC bias and DC current flow. The theoretical model employed to describe the impedance is presented in the next section.

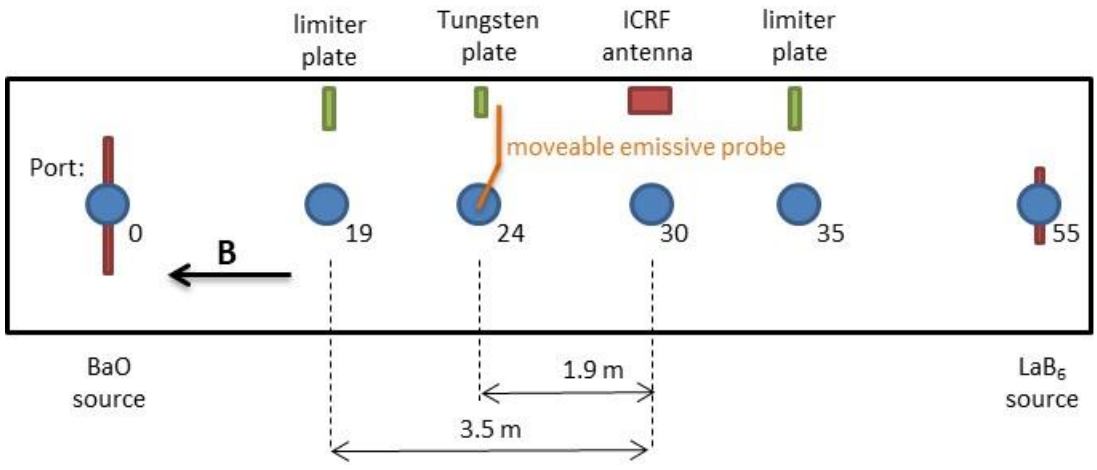

Fig. 1. Schematic of the LAPD geometry and experimental setup showing the top view, not to scale.

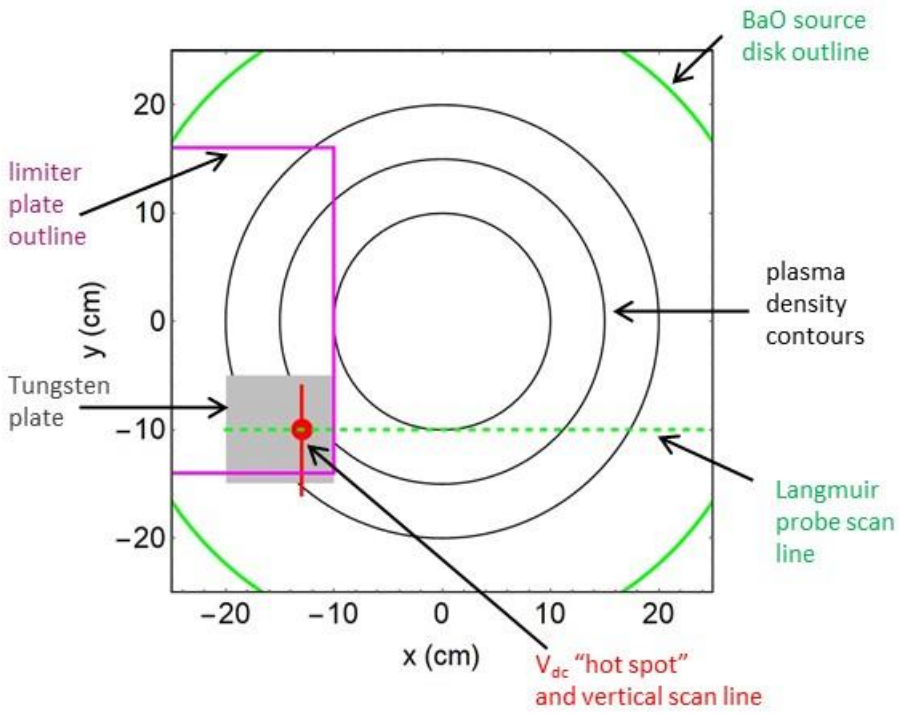

Fig. 2. Schematic of the LAPD geometry and experimental setup showing a cross-sectional view.

III. Theoretical model

A one-dimensional time-dependent micro-scale (i.e. Debye scale) RF sheath model was constructed in Ref. 38 using nonlinear fluid equations. The model geometry was that of a plasma immersed between symmetric capacitor plates. The main purpose of the model was to provide the RF sheath surface impedance and the rectified DC potential that result from a specified RF driving voltage, i.e. the oscillating voltage applied between the two plates. The model employed Maxwell-Boltzmann (MB) electrons at a single specified constant temperature T_e. The results of this model were later parametrized to a large number of code runs using asymptotic analysis and functional fits.[39]

In the present experiments, the sheaths at the two ends of the field line, the tungsten plate and the antenna, are not expected to be symmetric due to differences in geometry and excitation. Asymmetry is particularly important for the electron response, which in the MB limit causes the electrons to experience the entire field line simultaneously. This affects both the rectified DC potential and the electron contribution to the admittance, i.e. reciprocal of the impedance. Additionally, a warm electron tail was not treated in Refs. 38 and 39. For these reasons the electron

response needs to be generalized for application to the tungsten plate sheath of the present experiments.

The first difference is that here we regard the DC plasma potential at the entrance to the tungsten plate sheath as an *input* to the model rather than calculating it from the rectification effect on the local RF field. In practice we will see in Sec. IV that the DC potential is dominated by rectification at the antenna sheath, not the tungsten plate sheath. Second, we allow the electrons to have both a bulk MB contribution at $T_e = T_{e1}$ and a tenuous hot electron tail MB contribution at a higher temperature T_{e2}. Thus

$$n_e = n_{e0}(1-\beta)e^{e(\Phi-\Phi_u)/T_{e1}} + n_{e0}\beta e^{e(\Phi-\Phi_u)/T_{e2}} \tag{1}$$

where n_{e0} is the upstream density of the bulk plasma, Φ_u is the upstream potential, and β is the upstream density ratio of hot electrons to bulk electrons.

In Eq. (1) the electrostatic potential at the upstream sheath entrance (i.e. the plasma side of the sheath) is taken to be

$$\Phi_u \equiv \Phi_{dc} + \Phi_{rf}\cos(\omega t) \tag{2}$$

where Φ_{dc} is the specified DC potential and Φ_{rf} is the RF amplitude, all relative to the plate which is grounded, $\Phi_w = 0$. When Φ is positive and larger than a few T_{e1}, as will normally be the case, it confines most of the bulk electrons. The ones at high energy can escape to the plate or wall. The corresponding normalized current at the plate, obtained by integrating the first moment of the Maxwellian distributions over left-going velocities (i.e. those directed into the plate) is given by

$$\hat{J}_e \equiv \frac{J_e}{n_0 e c_{s1}} = -(1-\beta)\mu_1 e^{e(\Phi_w-\Phi_u)/T_1} - \beta\mu_2 e^{e(\Phi_w-\Phi_u)/T_2} \tag{3}$$

where $c_{s1} = (T_{e1}/m_i)^{1/2}$, $\mu_1 = (m_i/2\pi m_e)^{1/2}$ and $\mu_2 = (T_{e2}/T_{e1})^{1/2}\,\mu_1$.

The total DC current collected at the plate is J_e plus the ion saturation current $J_i = n_0 e c_{s1}$

$$\frac{J_{dc}}{n_0 e c_{s1}} = 1-(1-\beta)\mu_1 e^{-e\Phi_{dc}/T_1} - \beta\mu_2 e^{-e\Phi_{dc}/T_2} \tag{4}$$

where in Eq. (4) we assume that $\Phi_{rf} << \Phi_{dc}$.

The complex sheath admittance parameter y at frequency ω is defined as the ratio of the Fourier components of normalized current and voltage at the RF frequency ω,[38]

$$y = \frac{2\left\langle \hat{J}\cos\omega t\right\rangle}{\xi} + \frac{2i\left\langle \hat{J}\sin\omega t\right\rangle}{\xi} \tag{5}$$

where <…> indicates an average over an RF cycle, $\hat{J} = J/(n_0 e c_{s1})$ is the normalized total current (ion, electron and displacement) and $\xi = e|\Phi_{rf}|/T_{e1}$ is the normalized zero-to-peak amplitude of the RF voltage. Substituting the oscillatory form of Eq. (2) into Eqs. (3) and (5) and employing the Bessel function identity $e^{\xi\cos\varphi} = \sum_n I_n(\xi)e^{in\varphi}$ one arrives at the dimensionless electron admittance parameter

$$y_e \frac{4\pi\lambda_{de}}{\omega_{pi}} \equiv \hat{y}_e = \frac{2}{\xi}(1-\beta)\mu_1 \exp(-\hat{V}_{dc})I_1(\xi) + \frac{2}{\xi}\beta\mu_1\tau^{1/2}\exp(-\hat{V}_{dc}/\tau)I_1(\xi/\tau) \qquad (6)$$

where $\hat{V}_{dc} = e\Phi_{dc}/T_{e1}$, $\tau = T_{e2}/T_{e1}$ and $I_1(\xi)$ is the modified Bessel function of the first kind. Here, in dimensionless sheath units, time is normalized to the inverse ion plasma frequency $1/\omega_{pi}$, lengths are normalized to the Debye length $\lambda_{de} = c_{s1}/\omega_{pi}$, voltages to T_{e1}/e, and currents to $n_0 e c_{s1}$; hence, $y = J/\Phi$ is normalized to $\omega_{pi}/(4\pi\lambda_{de})$. In Eq. (6) CGS units are employed for y_e before converting to dimensionless form.

In this paper we will use the ion y_i and displacement y_d (i.e. capacitive) contributions to the admittance from Ref. 39, generalized to input $\hat{V}_{dc}$ instead of calculating it, together with Eq. (6) for the electron admittance. The total dimensionless RF admittance parameter is then

$$\hat{y} = \hat{y}_e + \hat{y}_i + \hat{y}_d \qquad (7)$$

Note that the impedance and/or admittance are given in the same dimensionless units in Refs. 38, 39 and in Eq. (6). The dimensionless admittance may be converted to a plate impedance in Ohms using

$$Z(\text{ohms}) = 9\times10^{11}\,\frac{4\pi\lambda_{de}(\text{cm})}{\omega_{pi}(\text{s}^{-1})A_n(\text{cm}^2)\hat{y}} \qquad (8)$$

where $A_n = 100$ cm^2 is the area of the plate normal to the magnetic field and the quantities λ_{de} and ω_{pi} employ the plasma parameters at the sheath upstream entrance. Experimental and model results which follow will be expressed in SI units of ohms, amperes and volts.

IV. Experimental results and model comparisons

A. Experimental position and antenna voltage scan

The basic characteristics of the plasma response in the present configuration are illustrated in Figs. 3 and 4. Figure 3 shows the plasma potential as measured along the red line in Fig. 2 for the case of no RF and full RF power, i.e. an RF antenna current of 503 A. For the no-RF case the DC plasma potential in front of the plate V_{dc} is between 0 and about 5 V as measured by the emissive probe. In the figure, the dashed line at y = –15 cm corresponds to the bottom edge of the

plate. The top edge of the plate is slightly beyond the upper limit of the measurements at y = –6 cm. From Langmuir probe measurements the plasma density in this region, which is in the shadow of the limiter, is approximately 1 to 2×10^{11} cm^{-3} and the bulk temperature is estimated as T_{e1} = 1 to 2 eV. Due to the low density and temperature in front of the plate, a more accurate determination of plasma parameters is not possible. As might be expected, the plasma potential under these conditions is on the order of a few T_e.

When the antenna is powered, the DC plasma potential maximizes along this scan line at a value of order V_{dc} ~ 80 V near y = –10 cm. This is the "hot spot" location where the analysis in Secs. IV B and C will be carried out. Although a high-resolution two-dimensional scan covering the entire plate is not available, this hot spot located at x = –13 cm, y = –10 cm is roughly the global maximum of V_{dc} over the plate surface. Figure 3 also shows the RF voltage V_{rf} along the same scan line. Here and in the following, V_{rf} is the RMS value of the total signal minus its DC value. Within a factor of $\sqrt{2}$ for a pure sinusoid, it is the experimental counterpart of the RF amplitude Φ_{rf} in the theory. Harmonics, discussed in Sec. IV C, are small, thus V_{rf} is almost all at the fundamental frequency of 2.5 MHz.

Note that V_{rf} is much smaller than V_{dc} and has a different spatial structure. This supports the assertion that the main source of V_{dc} is RF rectification at the antenna, not RF rectification at the plate. The direct rectification of V_{rf} at the tungsten plate in this low frequency limit will lead to a contribution[39] to the DC voltage of approximately $V_{dc} = (2^{3/2}/\pi)\, V_{rf} \sim 0.9\, V_{rf}$ which is too small to explain the observations. Instead it is likely that rectification of the larger RF voltages at the antenna is responsible for the observed DC voltage which is then transmitted along the field lines to the tungsten plate. In this paper we regard V_{dc} as an experimentally measured input. Its origin does not actually affect the modeling or conclusions.

The results of an RF antenna current (i.e. RF power) scan are shown in Figs. 4(a) and 4(b). Voltage data taken at the hot spot location is given in Fig. 4(a). Both the DC and RF voltages V_{dc} and V_{rf} scale approximately linearly with the RF antenna current I_{ant}. It is not surprising that V_{rf} is proportional to I_{ant} since the wave propagation is expected to be linear. The fact that V_{dc} is also linear with I_{ant} (except for a small thermal sheath offset) is consistent with sheath rectification when the RF potentials (in this case at the antenna) are much larger than T_e.[38, 39]

The currents collected at the plate flowing to ground are shown in Fig. 4(b) for the I_{ant} scan. When the RF is off, the plate collects negative current, i.e. an excess of electrons flow to the grounded plate, I_{dc} ~ –1 A. As the antenna current is raised I_{dc} passes through zero to positive values, reaching about I_{dc} ~ +1.5 A at maximum RF power. The RF current collected at the plate I_{rf} is approximately offset linear with I_{ant}. Note that the smallest I_{ant} for which there is data with the RF on is I_{ant} = 48 A.

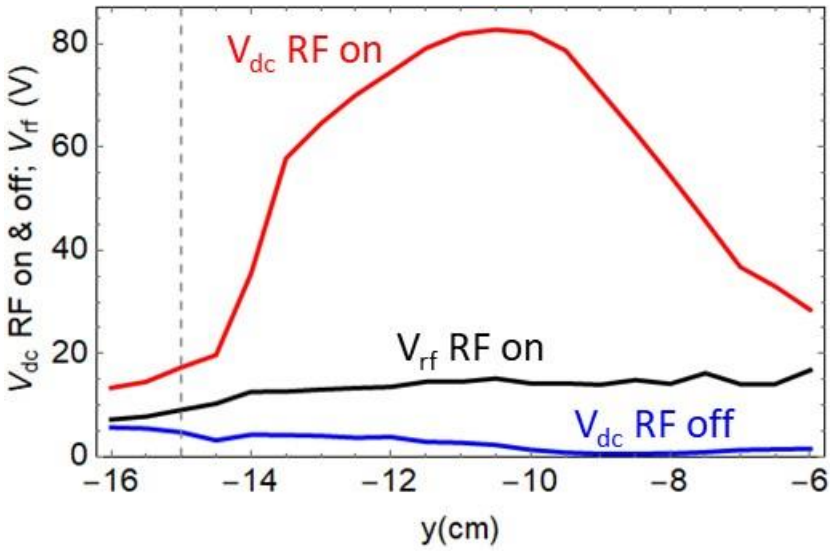

Fig. 3. DC and RF plasma potentials measured along the vertical red line in Fig. 2 for the case of no RF and full RF power. The dashed line at y = -15 cm corresponds to the edge of the plate.

B. DC analysis and modeling

The data shown in Figs. 3 and 4 is re-plotted in Fig. 5 in a solid red line, this time giving DC current as a function of DC plasma potential. The dashed lines show the result of the model of Sec. III using various parameter combinations. The first case, shown as a dashed green line is a best fit to the form of Eq. (4) with free fit parameters $I_{sat} = n_0 e c_{s1} A_n$, β, T_{e1} and T_{e2}. The result of the fit is I_{sat} =1.58 A, $\beta = 0.0059$, $T_{e1} = 0.97$ eV and $T_{e2} = 43$ eV. Using the area of the plate, $A_n = 100$ cm^2, the fitted $J_{sat} = 158$ A/m^2. On the other hand, assuming $n_e = 2\times10^{11}$ cm^{-3} and $T_{e1} = 1$ eV one obtains $J_{sat} = n_0 e c_{s1} = 157$ A/m^2. Consequently, this best fit is remarkably consistent with the Langmuir probe estimates of the bulk density and temperature, and with the expected ~ 50 eV hot electron temperature. The remaining dashed curves illustrate the parameter sensitivity in relation to the underlying physics.

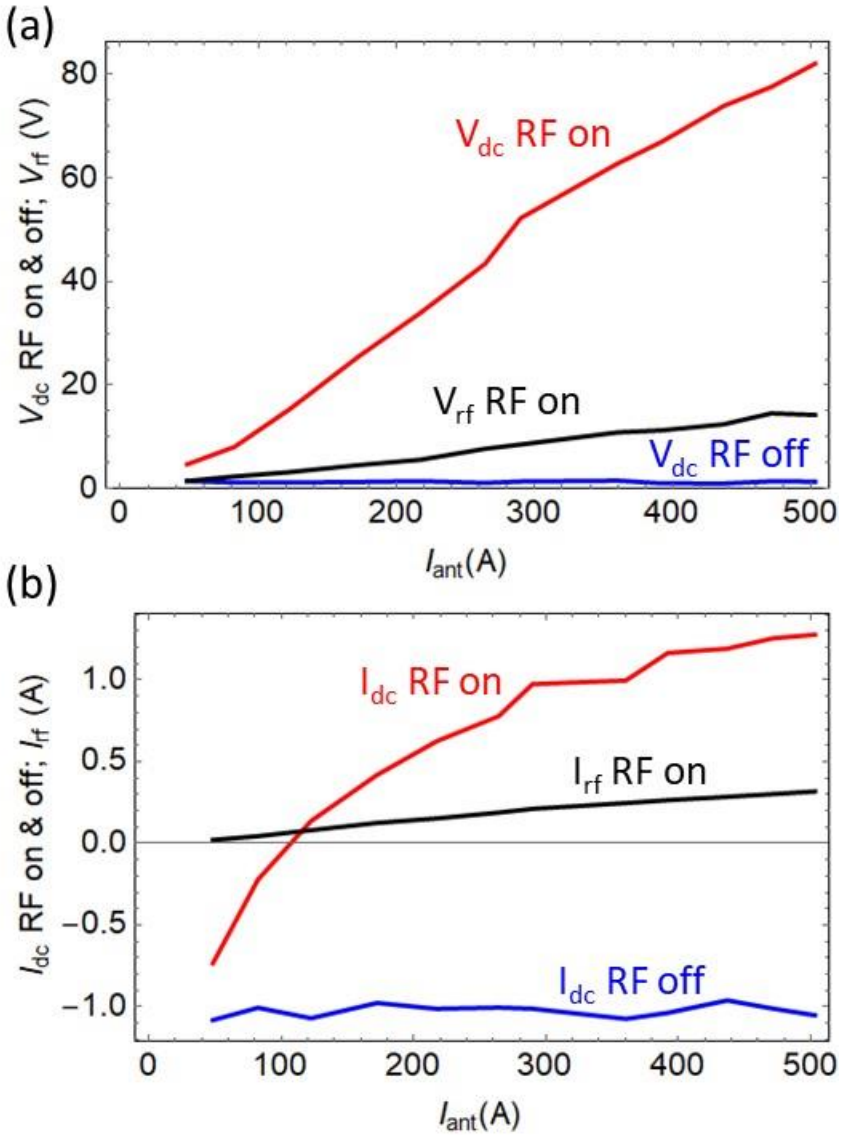

Fig. 4. Results of an RF antenna current (power) scan: (a) DC and RF plasma potentials at the location of the hot spot and tungsten plate and (b) DC and RF plate current in amps. The case with no RF, obtained during the plasma discharges prior to the RF pulse, is also shown.

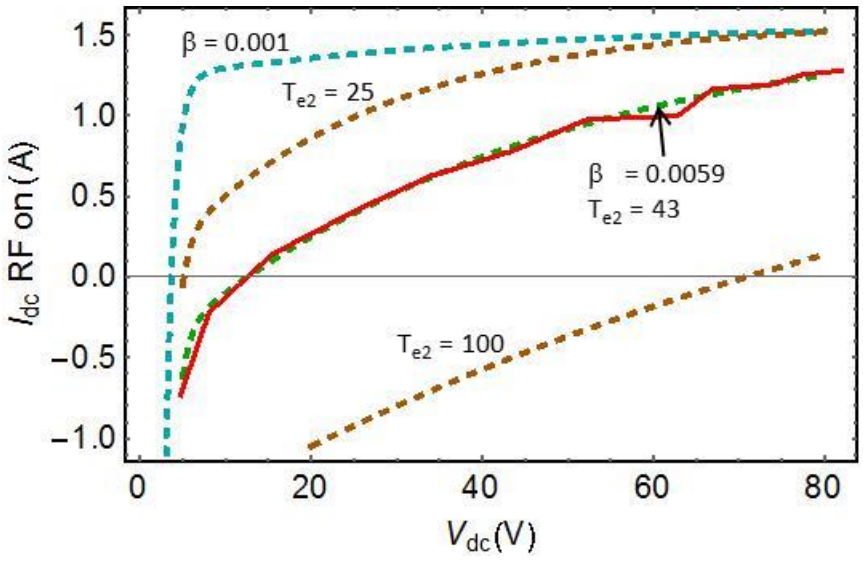

Fig. 5. DC current-voltage characteristic for the tungsten plate sheath during the antenna current (power) scan. The solid red line is the experimental data, and the dashed lines are from the model showing the best fit and the sensitivity to parameter choices (see text).

Keeping the other parameters the same as for the best fit, the uppermost dashed curve is the result for a very low, almost negligible fraction of hot electrons, $\beta = 0.001$. At all but the very lowest values of V_{dc} the plasma potential traps all of the thermal electrons. The hot electron current is almost negligible and only ions can escape to the plate. Therefore, without hot electrons and for $V_{dc} > 5$ eV the current is essentially at the ion saturation level. Thus, a poor fit to the data results when the hot electron population is too small.

If instead of using base case values the hot electron temperature is reduced from 47 eV to 25 eV with other parameters unchanged, the shape is acceptable but the resulting decrease in lost hot electron current causes the curve to lie above the data. Conversely, if $T_{e2} = 100$ eV too many hot electrons are lost and the model predicts a current that is net negative over most of the plotted range of V_{dc}. These cases show that while the electron density is mostly determined by the bulk T_{e1} electrons, the electron current is mostly determined by the hot T_{e2} electrons. Finally note that the $I_{dc} = 0$ floating plate condition in the experiment occurs at $V_{dc} \sim 12$ V which would be impossible if bulk $T_{e1} \sim 1 – 2$ eV electrons were the only electron species. A floating potential of 12 V necessarily implies an electron species with an energy at least that high, and several time higher if the component is a Maxwellian.

Having established the characteristics of the background plasma, we are now in a position to proceed to the main point of this paper, the response of the sheath to upstream RF oscillations.

C. RF data analysis

As discussed in Sec. II, the emissive probe and Pearson current probe diagnostic systems are able to time-resolve the phase of the RF component of the plasma potential and plate current. An example of these signals is shown in Fig. 6(a). Figure 6(b) replots the same data as a parametric plot where time traces out the signal in the phase plane of (V_{rf}, I_{rf}). The time trace is indicated with the thin red line. From this plot it is possible to deduce the magnitude and phase of the complex sheath impedance $Z = V_{rf}/I_{rf}$ by fitting an ellipse, shown in the figure with a thick black line. The detailed fitting procedure is described next.

A 3 ms time series of signals during the RF pulse was employed. This long time series, digitized at 25 MHz (with Nyquist frequency well above RF frequency of 2.5 MHz) was first subdivided into segments of length 8 μs as shown in Fig. 6(a). A band-pass filter was then applied to each segment, passing frequencies in the range 0.8 ω to 1.3 ω. The filtering operation primarily removed slow oscillations in the plasma due to turbulence, ~ 0 to 10 kHz, which competed with the signals at very low RF power. An ellipse in the (V_{rf}, I_{rf}) plane was then fit to these data points. Figure 6(c) illustrates what the ellipses would look like for phase differences of 0, π/4, π/2 and π. Thus, the orientation of the ellipse gives the phase difference between V_{rf} and I_{rf}, i.e. the phase of the impedance, and the amplitude ratio of V_{rf} and I_{rf} gives the magnitude of the impedance.

We note in passing that the raw RF signals (i.e. before band-pass filtering) were dominated by the fundamental. The ratio of the Fourier amplitudes of the (2ω) harmonic to the fundamental at the highest RF power was 0.078 for the voltage and 0.085 for the current. At the lowest RF power these ratios were less than 0.04.

For a given antenna current, the complex impedance analysis was carried out for all the time segments in the longer data array and the mean and standard deviation were recorded. This procedure was then repeated for each I_{ant} in the antenna current scan. The results are shown in Figs. 7 and 8. Figure 7 presents the analyzed data with black filled circles and error bars, giving the mean and standard deviation respectively. Data is plotted against V_{dc} which, as we have seen, varied monotonically, and almost linearly with I_{ant}. The dashed curves in Fig. 7 are the results of a theoretical model to be discussed in the remainder of this section.

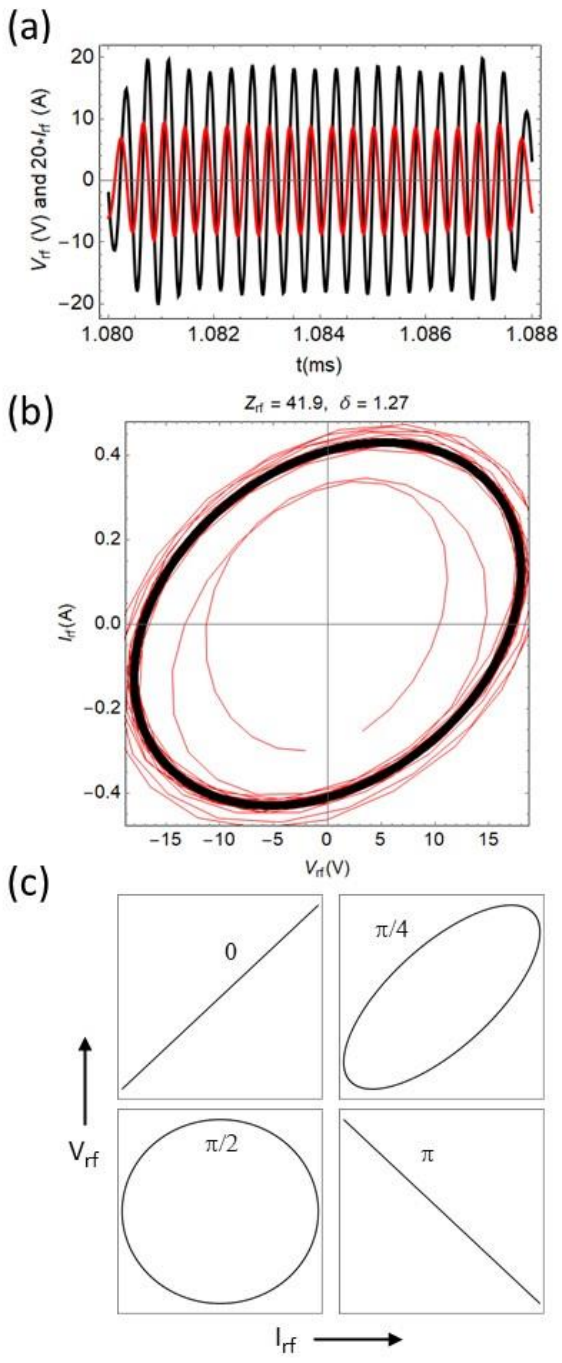

Fig. 6. (a) Overlaid time traces of RF plasma potential (black) and RF plate current (red) for a small time-sample. The RF plate current has been multiplied by a factor of 20 to make it visible on the same scale. (b) The same data shown as a parametric plot in the (V_{rf}, I_{rf}) plane with time tracing out the thin red lines. The thick black line is the best fit ellipse. (c) Simulated ellipse shapes in the same (V_{rf}, I_{rf}) plane for phase differences of 0, $\pi/4$, $\pi/2$ and π.

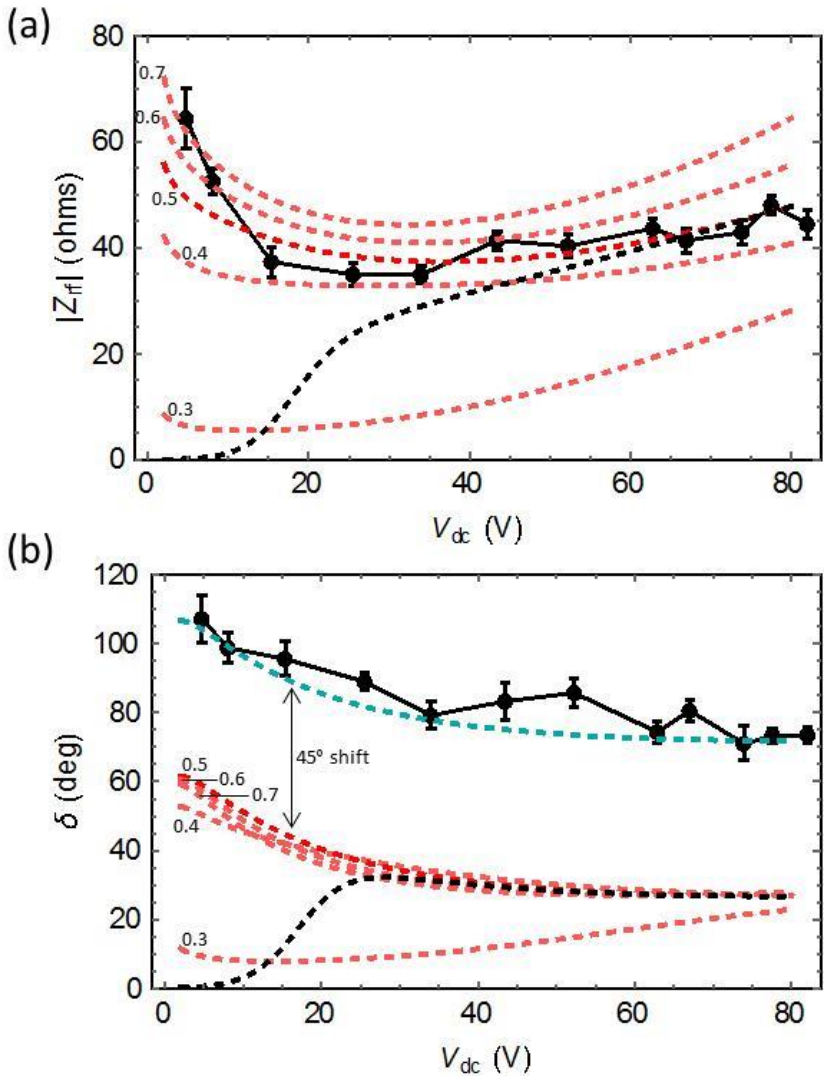

Fig. 7. Experimental data for the complex impedance (black filled circles and error bars) and results of model calculations described in the text (dashed curves): (a) magnitude of the RF sheath impedance and (b) phase of the RF sheath impedance.

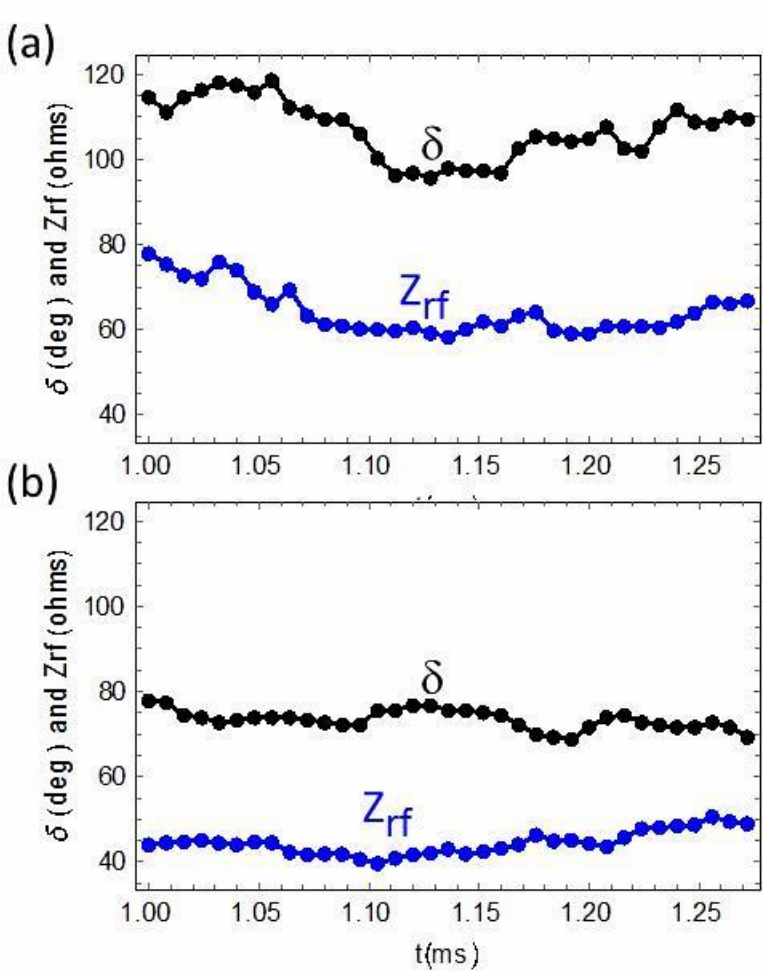

Fig. 8. Time variation of the magnitude (blue) and phase (black) of the experimental sheath impedance for several 8 μs sub-series at (a) the lowest RF power, I_{ant} = 48 A and (b) the highest RF power I_{ant} = 503 A.

Figure 8 shows the analyzed impedance data for several 8 μs sub-series at the lowest and highest RF powers. There is some variation in the magnitude and phase of sheath impedance under what are nominally similar conditions. In the low power case $Z_{rf} = 64 \pm 6$ ohms and $\delta = 107 \pm 7$ degrees. By comparison the high-power case yields $Z_{rf} = 44 \pm 3$ ohms and $\delta = 73 \pm 2$ degrees. The variation is likely attributable to turbulence which would affect the local density and temperature at the plate. Also noticeable is that the variations in Z_{rf} and δ are positively correlated in the low power case with a correlation coefficient of +0.76. In contrast, the high-power case has a negative and somewhat weaker correlation coefficient of −0.50. These observations will be discussed in the next section, Sec. IV D.

D. RF sheath impedance modeling

As we have seen both V_{dc} and V_{rf} change during the antenna voltage scan. In modeling the sheath impedance data, it is useful to parametrize V_{rf} in terms of V_{dc} because theoretically, Z depends on both quantities through Eqs. (6) – (8). Figure 9 shows the experimental relationship between V_{rf} and V_{dc} in a solid red line and a linear fit in dashed green that will be employed in the modeling, namely

$$\xi = \sqrt{2}\,\frac{eV_{rf}}{T_{e1}} = \sqrt{2}\,\frac{eV_{dc}}{T_{e1}}\,\frac{14}{80} \tag{9}$$

where $\sqrt{2}$ converts the RF voltage V_{rf} into the 0-peak value required for Eq. (6).

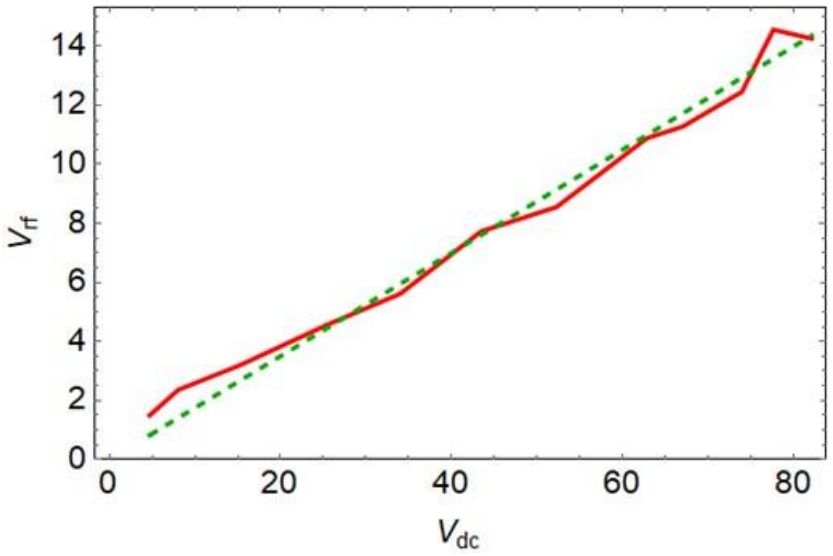

Fig. 9. Experimentally observed (solid red) variation of the RF plasma potential V_{rf} with the DC plasma potential V_{dc} during an antenna power scan, and a linear analytic fit (dashed green) used in the modeling.

To complete the inputs required for calculating an RF impedance from the sheath model it is required to specify n_e, T_{e1}, β, T_{e2} and an average V_{dc} over the plate. This latter quantity, $V_{dc,avg}$ will be different from, and smaller than, V_{dc} at the hot spot, i.e. $V_{dc,avg} = \alpha_{dc} V_{dc}$ with $\alpha_{dc} < 1$. A rough estimate based on the one-dimensional scan shown in Fig. 3 suggests $\alpha_{dc} \sim 0.5$; in the following, we also explore the sensitivity to α_{dc}. Other parameters are $n_e = 2\times10^{11}$ cm^{-3}, $T_{e1} = 1$ eV, $\beta = 0.006$, and $T_{e2} = 50$ eV. The resulting RF sheath impedance for $\alpha_{dc} = 0.5$ is shown as a dashed black line in Fig. 7. This model shows good agreement with the magnitude of Z_{rf} at the higher values of V_{dc} but departs significantly at low RF power (low V_{dc}). The magnitude of the

model impedance goes to zero because at low enough V_{dc} many electrons have enough energy to escape the DC confining sheath potential and reach the plate making the electron current large and the impedance small. Under these conditions the impedance is also real ($\delta = 0$), since the electron current from Eq. (6) is in phase with the RF voltage. The phase discrepancy between the model and the data, and the modeling shown in the dashed red and cyan curves will be discussed next.

To understand a possible reason for the magnitude discrepancy at all but the highest values of V_{dc}, recall the specific geometry of the experiment: the plasma that carries the RF waves, namely between the plate and the antenna, is also shadowed by the limiter plate from the hot electrons emitted by the BaO source. This is sketched in Fig. 10. At high power, and hence high V_{dc} this region of the plasma is biased strongly positive. However, there are also variations of this positive V_{dc} across the field lines (since different field lines have different contact points with the antenna and its rectified voltages). The result is RF convection driven by E×B drifts, as previously documented in other experiments both on tokamaks[60-62,68] and on LAPD.[33] This convection can drive cross-field radial transport that carries hot electrons into the region between the plate and the antenna. Hot electrons entering this region can subsequently be trapped in the parallel direction by the confining potential.

The eddy convection time is estimated as $\tau_{eddy} = L_\perp/v_E$ where $L_\perp$ is a characteristic perpendicular scale length of the eddy and $v_E = c\Phi/(BL_\perp)$ is the E×B velocity for a peak eddy potential of order Φ. On the other hand, the parallel bounce time between the plate and the antenna and back again for a hot electron is $\tau_{||} = 2L_{||}/v_{te2}$ where v_{te2} is the hot electron thermal velocity. Their ratio is given by

$$\frac{\tau_{eddy}}{\tau_{||}} = \frac{BL_\perp^2 v_{te2}}{2cL_{||}\Phi} \rightarrow \left(\frac{L_\perp(\text{cm})}{5.4}\right)^2 \tag{10}$$

where the last estimate employs the values B = 1 kG, T_{e2} = 50 eV, $L_{||}$ = 550 cm, and Φ = 80 V = 80/300 statV. Judging from Fig. 3, an 80 V eddy of scale size $L_\perp \sim 5$ cm is entirely reasonable, allowing significant cross-field transport in a single bounce time. Furthermore, electrons that are electrostatically trapped between the plate and the antenna can undergo multiple bounces allowing even more time for cross-field transport. Note, that the estimate for the E×B velocity of $v_E = 1.6\times10^6$ cm/s is on the same order as the measured value of 1.1×10^6 cm/s in a previous experiment with similar parameters (see Fig. 3 of Ref. 33) and close to the sound speed.

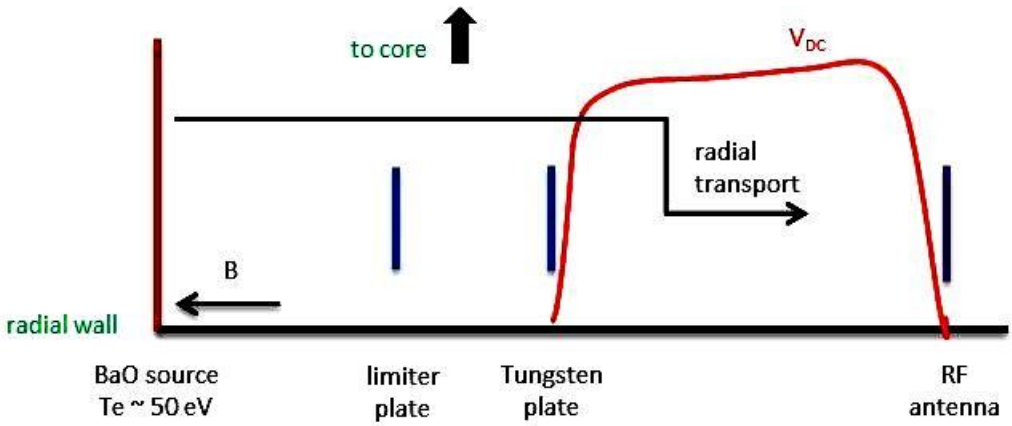

Fig. 10. Sketch of the axial geometry showing the variation of V_{dc} which can trap electrons, and the postulated radial transport which can populate the region between the tungsten plate and the antenna with hot electrons from the BaO source.

Thus, it appears possible that hot electrons are present on both sides of the plate, and in particular on the RF side, when the RF voltage is high enough to induce large convective cross-field transport. Conversely at low power, the convection-induced radial transport of hot electrons becomes small, and the confining potential becomes too low to trap the 50 eV electrons. As a result, at the lowest powers we postulate that there are essentially no hot electrons in the RF region, and furthermore there is very little bulk plasma there because the hot electrons are required to ionize the neutral ^{4}He gas. It is then not surprising that the RF current to the plate disappears resulting in a high RF impedance at low power.

It is clear that a predictive model of this effect would require physics that is well beyond the scope of this paper. However, it is possible to verify the reasoning by proposing an ad-hoc decrease of plasma and hot electron density and plasma temperature. We let

$$\begin{aligned} n_e &= n_{e0}\, f(V_{dc} / V_{dc0}) \\ T_e &= T_{e0}\, f(V_{dc} / V_{dc0}) \end{aligned} \tag{11}$$

where the ad-hoc function $f(x) = x \exp(1-x)$ is plotted in Fig . 11, $V_{dc0} = 80$ V, $n_{e0} = 2\times10^{11}$ cm^{-3} and $T_{e0} = 1$ eV. Note that the hot electron density $\beta n_{e0} f(V_{dc}/V_{dc0})$ decreases to zero as $V_{dc} \to 0$ together with the bulk electron density.

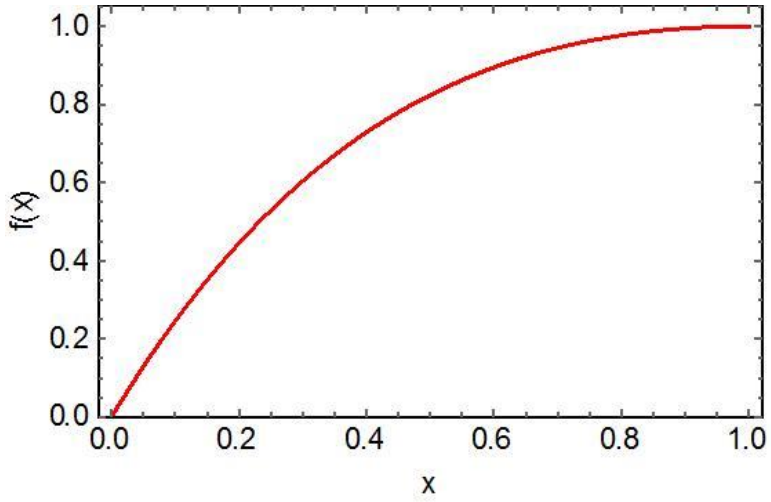

Fig. 11. Assumed function form describing the decrease of plasma density and temperature at low RF power (antenna voltage) $\propto$ x.

Results of this model are shown as the dashed red curves in Fig. 7. The dark red dashed curve is for $\alpha_{dc} = 0.5$; the lighter dashed red curves are for α_{dc} ranging between 0.3 and 0.7 with values indicated next to each curve. Now, as expected, the magnitude of the impedance in Fig 7(a) increases for small and decreasing V_{dc}. The degree of quantitative agreement with the data for $\alpha_{dc} = 0.5$ is fortuitous since the function f(x) is ad-hoc, but the qualitative features of the model calculation support the hypothesis that the plasma in front of the plate essentially disappears at the lowest power levels. The phase variation of the impedance predicted by the model, and shown by the red dashed curves in Fig 7(b), signifies a change from mostly resistive impedance at high power, to more capacitive impedance at low power: a purely capacitive sheath would have $\delta = \pi/2$ in our phase convention. The resistive component of the response comes from the RF electron current, which according to Eq. (6) is in phase with the RF voltage. As the (bulk and hot) electron and ion densities drop, so do the electron and ion currents until only displacement current remains and the sheath is essentially capacitive.

The model calculations only provide a reasonable fit to the experimentally measured phase when they are shifted by about 45 degrees, as indicated by the teal dashed curve in Fig. 7(b). This phase shift is conjectured to arise from details of the Pearson current probe and emissive probe systems including the different lengths of cable connecting these probes to the data digitizing system. An experimental calibration of this diagnostic-induced phase shift was not available. However, a known systematic error is the inherent phase lag of the reported current of the current meter from the true phase, and is quoted by the manufacturer (at the 2.5 MHz used in the experiment) to be 6 degrees (0.1 Radians). The voltage monitor used does not have a measurable phase discrepancy at the same frequency. To further estimate an overall experimental offset in the

phase difference, we note that the cables used in this experiment connecting the current probe and voltage probe to the data recording hardware differ in length by of order 10 m. At 2.5 MHz the RG58 cables used would have an in-cable wavelength of 83 m. Thus, we would expect the phase correction due to this effect to be of order $2\pi\times10/83 = 0.76$ rad or about 43 degrees. The combined uncertainties are consistent with the assumed phase shift.

Finally returning to Fig. 8(a), taken at low power, it was noted previously that the magnitude and phase of the RF sheath impedance shows some degree of positive time correlation. We postulated that turbulent cross-field transport is responsible for populating the relevant flux tubes with hot electrons, relevant being the ones connecting to the tungsten plate on the RF antenna side. At low RF power, the RF-driven E×B transport becomes small, but low frequency turbulence, routinely observed in LAPD,[69] remains. It is plausible that the resulting intermittent fluctuations in the 0 – 10 kHz range, consistent with the time scales in Fig. 8, determine the plasma density and temperature as well as the hot electron fraction in front of the plate under these conditions. The changes in the magnitude of Z_{rf} are roughly consistent with a relative density fluctuation of 10% - 20%. The observed correlation between $|Z_{rf}|$ and δ is not unreasonable since both depend, in different ways, on the fluctuating plasma conditions. The sign of the correlation in the low and high-power cases is not understood at this time; however, the fact that this sign is different at low and high power is suggestive of different physical processes governing the turbulence and/or the sheath physics at these different power levels.

Before closing this section, it is worth noting that there is another mechanism besides RF convection that can produce a hot electron population that scales with RF power, and hence with V_{dc}. That mechanism is direct ICRF heating of the electrons by wave-particle interaction. Significant electron heating requires $\omega/|k_{||}v_{te}| \sim 1$ or smaller. For 1 eV electrons at the RF frequency of 2.5 MHz this condition requires $|k_{||,1}| \geq 0.36$ cm^{-1}. The corresponding parallel scale length is $L_{||,1} = \pi/|k_{||,1}| \leq 8.7$ cm. The width of the antenna current strap is 6 cm (in the direction parallel to B) and the width of the antenna box (also parallel) is 10 cm. The single strap antenna will create a broad spectrum, peaking at $k_{||} = 0$ and extending up to and beyond $k_{||} = \pi/6$ cm^{-1}. Thus, it is reasonable that the antenna near fields could directly interact with and heat 1 eV electrons. Clearly this source of hot electrons would also disappear at low power and its effect on the RF impedance would be qualitatively similar to our ad-hoc treatment of RF convection. At high power, the 50 eV electrons may also be heated and or sustained by RF wave-particle interaction from the fast wave. For these electrons the critical parallel wavenumber is $k_{||,50} > 0.051$ cm^{-1} corresponding to full wavelength of $2\pi/k_{||,50} = 62$ cm. The typical parallel wave length of the fast wave measured in past LAPD experiments is 60 to 90 cm.[70] A simple dispersion estimate would suggest that the $k_{||} > 0.05$ cm^{-1} would be limited from propagation by the right-hand cutoff.

V. Discussion and conclusions

In this paper we have described an experiment that has, within some limitations and assumptions, verified the modeling of the DC and RF sheath impedance in the large magnetized plasma of LAPD. Specifically, we were able to measure and model RF sheaths on field lines impacting a grounded plate at one end and connected to an RF antenna at the other end. In this configuration the RF voltages at the plate were not the primary driver of the rectified DC sheath potential: the primary DC sheath driver came instead from the rectification at the antenna. This made it possible to measure the RF sheath impedance at the plate as a function of DC sheath voltage, by varying the RF voltage applied to the antenna.

The main conclusions of this paper stem from Eqs. (4) and (6) for the modeling, and from Figs. 5 and 7 which compare the modeling to experimental data. In Fig. 5 we showed that the DC sheath characteristics at the plate could be modeled by including a tenuous hot electron component associated with the emissive cathode used in LAPD for plasma production. The hot electron component that best fit that data was seen to be an unimportant contributor to the plasma density, at an upstream density ratio of about 0.006, but made an important, order unity, contribution to the current collected at the plate.

Using information deduced about the background plasma from the DC analysis, an RF sheath impedance analysis was carried out and compared with data in Fig. 7. It was shown in Fig. 7(a) that at the highest DC voltages, V_{dc} ~ 40 to 80 V, a basic model of the RF impedance fit the magnitude of the measured impedance rather well. This basic model included contributions from both the bulk and hot electron admittances as well as smaller contributions from the ion and displacement admittances.

At lower DC voltages, in the range V_{dc} ~ 5 to 40 V additional assumptions were required to model the data. It was postulated that RF-driven convection was necessary to transport hot electrons into the region in front of the plate where the RF waves determining the RF impedance were present. At low V_{dc}, RF convection is expected to weaken, resulting in the loss of both hot electrons and indeed the bulk plasma, which is created by the hot electrons. This effect was qualitatively modeled and shown to reproduce the main trend in the data as V_{dc} was reduced, namely an increase in the magnitude of the RF impedance. It was noted that hot electrons could also be created by RF wave-particle interactions in the SOL. These would also scale with RF power, and would produce the same qualitative trend of the impedance at low V_{dc} as our RF convection model.

It is important to note that in contrast to the RF impedance, for the DC impedance (i.e. the DC current vs. DC voltage characteristic in Fig. 5) the plate can collect hot electrons on the back side facing the BaO source. As a result, the DC current-voltage characteristic is not expected to be

sensitive to the cross-field transport of electrons to the region in front of the plate. Indeed, this effect was not required to successfully model the DC response in Fig. 5.

Returning to the RF impedance, an attempt was also made to measure and model its complex phase angle. Results were presented in Fig. 7(b). The modeling predicted a mostly resistive impedance at high V_{dc} (i.e. phase angle δ close to zero) but acquired a significant capacitive character (δ approaching $\pi/2$) at very low V_{dc}. These trends could be understood from the postulated mechanism for RF driven convection and cross-field transport of the hot electrons. The net modeled change in phase angle between low (V_{dc} = 5) and high (V_{dc} = 80 V) was very similar to the experimental measurements; however, an overall offset in phase of about $\pi/4$ was present. This phase shift was estimated to be consistent with combined experimental uncertainties.

Taken as whole, these results confirm the sheath impedance modeling of Refs. 38 and 39 with some modifications and extensions described in Sec. II. Specifically, the plasmas considered here required (i) that the DC sheath voltage be treated as an independent input parameter, and (ii) that a hot electron component be retained in addition to the colder bulk electrons. Both extensions may prove of interest for RF sheath modeling in tokamaks and other fusion-relevant devices. Although emissive cathodes are not used for plasma production in tokamaks, the presence of an energetic electron component in the scrape-off layer is possible, if not likely. The conditions for complete thermalization of electrons transported from the hot closed surface regions may not be well satisfied. Furthermore, when lower hybrid wave power is employed, there can be direct heating of electrons causing hot tails.

The type of magnetically connected RF sheath studied here, may be relevant to RF sheaths in fusion experiments as well. The DC sheath voltage on remote surfaces that *are* magnetically connected to a distant antenna may be the result of RF voltage rectification at the antenna rather than RF rectification at the remote surface. In principle, both sources of rectification should be taken into account, and the dominance of one over the other would depend on both wave propagation physics determining the RF amplitude at the remote surface and on the global DC circuits in the plasma (parallel and cross-field) and vessel walls. On the other hand, far-field RF sheaths that are *not* magnetically connected to an antenna, but instead result from RF waves impacting the surface, are yet a separate topic. As discussed in the references given in the introduction, both slow waves and fast waves incident on a surface are expected on theoretical grounds to drive RF sheaths; the fast wave requires in general an oblique magnetic field. Direct verification of these types of sheaths and their properties in dedicated experiments would be a useful step forward.

It is hoped that the present work, in combination with additional study of various RF sheath geometries and in a variety of parameter regimes, can ultimately provide verified and robust models for predicting and analyzing ICRF sheath interactions in fusion devices.

Acknowledgements

This material is based upon work supported by the U.S. Department of Energy Office of Science, Office of Fusion Energy Sciences under Award Numbers DE-AC05-00OR22725 sub-contract 4000158507 and DE-FG02-97ER54392. Discussions with T. Carter, G. Bal, R. Barnett and members of the RF SciDAC project (Center for Simulation of Wave-Plasma Interactions) are gratefully acknowledged. The digital data for this paper can be found in Ref. 71. Additional data that support the findings of this study are available from the corresponding author upon reasonable request.

References

[1] R. Chodura, Phys. Fluids **25**, 1628 (1982).

[2] R. H. Cohen and D. D. Ryutov, Phys. Plasmas **5**, 808 (1998).

[3] K.-U. Riemann, Phys. Plasmas **1**, 552 (1994).

[4] P.C. Stangeby, Nucl. Fusion **52**, 083012 (2012).

[5] F. W. Perkins, Nucl. Fusion **29**, 583 (1989).

[6] J. R. Myra, D. A. D'Ippolito, and M. J. Gerver, Nucl. Fusion **30**, 845 (1990).

[7] J.R. Myra, D.A. D'Ippolito, D.A. Russell, L.A. Berry, E.F. Jaeger and M.D. Carter, Nucl. Fusion **46** S455 (2006).

[8] M. Elias, D. Curreli, T. G. Jenkins, J. R. Myra, and J. Wright, Phys. Plasmas **26**, 092508 (2019).

[9] L. Colas, L. Costanzo, C. Desgranges, S. Brémond, J. Bucalossi, G. Agarici, V. Basiuk, B. Beaumont, A. Bécoulet and F. Nguyen, Nucl. Fusion **43**, 1 (2003).

[10] J.-M. Noterdaeme and G. Van Oost, Plasma Phys. Control. Fusion **35,** 1481 (1993).

[11] D.A. D'Ippolito, J. R. Myra, M. Bures, and J. Jacquinot, Plasma Phys. Cont. Fusion **33**, 607 (1991).

[12] V. Bobkov, F. Braun, L. Colas, R. Dux, H. Faugel, L. Giannone, A. Herrmann, A. Kallenbach, H.W. Müller, R. Neu, J.-M. Noterdaeme, Th. Pütterich, G. Siegl, E. Wolfrum, ASDEX Upgrade Team, Journal of Nuclear Materials **415**, S1005 (2011).

[13] G. Urbanczyk, L. Colas, X.J. Zhang, W. Helou, Y.P. Zhao, M. Goniche, X. Z. Gong, E. Lerche, G. Lombard, Q.C. Ming, et al., 23rd Topical Conference on Radiofrequency Power in Plasmas, May 14-17, 2019, Hefei, China, paper I3.5 [AIP Conf. Proceedings].

[14] S. J. Wukitch, M. L. Garrett, R. Ochoukov, J. L. Terry, A. Hubbard, B. Labombard, C. Lau, Y. Lin, B. Lipschultz, D. Miller, M. L. Reinke, D. Whyte, and Alcator C-Mod Team, Phys. Plasmas **20**, 056117 (2013).

[15] J. Jacquot, D. Milanesio, L. Colas, Y. Corre, M. Goniche, J. Gunn, S. Heuraux, and M. Kubič, Phys. Plasmas **21**, 061509 (2014).

[16] C. M. Qin, Y. P. Zhao, H. Q. Wang, X. J. Zhang, B. N. Wan, J.-M. Noterdaeme, F. Braun, V. Bobkov, H. Kasahara, E. H. Kong, L. Wang, Y. Shuai, Z. X. He, B. J. Ding, ICRF Team and EAST Team, Plasma Phys. Control. Fusion **55**, 015004 (2013).

[17] Y. Corre, M. Firdaouss, L. Colas, A. Argouarch, D. Guilhem, J. Gunn, C Hamlyn-Harris, J. Jacquot, M. Kubic, X. Litaudon, M. Missirlian, M. Richou, G. Ritz, D. Serret and K. Vulliez, Nucl. Fusion **52**, 103010 (2012).

[18] I. Cziegler, J. L. Terry, S. J. Wukitch, M. L. Garrett, C. Lau and Y. Lin, Plasma Phys. Control. Fusion **54**, 105019 (2012).

[19] R.J. Perkins, J.-W. Ahn, R.E. Bell, A. Diallo, S. Gerhardt, T.K. Gray, D.L. Green, E.F. Jaeger, J.C. Hosea, M.A. Jaworski, B.P. LeBlanc, G.J. Kramer, A. McLean, R. Maingi, C.K. Phillips, M. Podesta, L. Roquemore, P.M. Ryan, S. Sabbagh, F. Scotti, G. Taylor and J.R. Wilson, Nucl. Fusion **53**, 083025 (2013).

[20] R. Ochoukov, D. G. Whyte, D. Brunner, D. A. D'Ippolito, B. LaBombard, B. Lipschultz, J. R. Myra, J. L. Terry and S. J. Wukitch, Plasma Phys. Control. Fusion **56**, 015004 (2014).

[21] P. Jacquet, L. Colas, M.-L. Mayoral, G. Arnoux, V. Bobkov, M. Brix, P. Coad, A. Czarnecka, D. Dodt, F. Durodie, et al., Nucl. Fusion **51**, 103018 (2011).

[22] L. Colas, J. Jacquot, S. Heuraux, E. Faudot, K. Crombé, V. Kyrytsya, J. Hillairet and M. Goniche, Phys. Plasmas **19**, 092505 (2012).

[23] D. N. Smithe, D. A. D'Ippolito, and J. R. Myra, AIP Conference Proceedings **1580**, 89 (2014).

[24] N. Bertelli, E.F. Jaeger, J.C. Hosea, C.K. Phillips, L. Berry, S.P. Gerhardt, D. Green, B. LeBlanc, R.J. Perkins, P.M. Ryan, G. Taylor, E.J. Valeo and J.R. Wilson, Nucl. Fusion **54**, 083004 (2014).

[25] D. Van Eester, K. Crombé and V. Kyrytsya, Plasma Phys. Control. Fusion **55**, 055001 (2013).

[26] J.R. Myra and D.A. D'Ippolito, Plasma Phys. Controlled Fusion **52**, 015003 (2010).

[27] D. A. D'Ippolito, J. R. Myra, R. Ochoukov, and D. G. Whyte, Plasma Phys. Control. Fusion **55**, 085001 (2013).

[28] H. Kohno and J. R. Myra, Phys. Plasmas **26**, 022507 (2019).

[29] H. Kohno and J. R. Myra, Comput. Phys. Commun. **220**, 129 (2017).

[30] H. Kohno, J. R. Myra, and D. A. D'Ippolito, Phys. Plasmas **22**, 072504 (2015); ibid, Phys. Plasmas **23**, 089901 (2016).

[31] W. Tierens, J. Jacquot, V. Bobkov, J.M. Noterdaeme, L. Colas and The ASDEX Upgrade Team, Nucl. Fusion **57**, 116034 (2017).

[32] L Lu, L Colas, J Jacquot, B Després, S Heuraux, E Faudot, D Van Eester, K Crombé, A Křivská, J-M Noterdaeme, W Helou and J Hillair, Plasma Phys. Control. Fusion **60**, 035003 (2018).

[33] M. J. Martin, W. Gekelman, B. Van Compernolle, P. Pribyl, and T. Carter, Phys. Rev. Lett. **119**, 205002 (2017).

[34] J. R. Myra, D. A. D'Ippolito and M. Bures, Phys. Plasmas **1**, 2890 (1994).

[35] E.F. Jaeger, L.A. Berry, J.S. Tolliver, D.B. Batchelor, Phys. Plasmas **2**, 2597 (1995).

[36] D. A. D'Ippolito and J. R. Myra, Phys. Plasmas **13**, 102508 (2006).

[37] W. Tierens, G. Urbanczyk, L. Colas, and M. Usoltceva, Phys. Plasmas **26**, 083501 (2019).

[38] J. R. Myra and D. A. D'Ippolito, Phys. Plasmas **22**, 062507 (2015).

[39] J. R. Myra, Phys. Plasmas **24**, 072507 (2017).

[40] C. Nieter and J. R. Cary, J. Comp. Phys. **196**, 448 (2004).

[41] R. Khaziev and D. Curreli, Comp. Phys. Commun. **229**, 87 (2018).

[42] T. G. Jenkins and D. N. Smithe, Plasma Sources Sci. Technol. **24**, 015020 (2015).

[43] J. R. Myra, D. Curreli, M.T. Elias and T. G. Jenkins, 23rd Topical Conference on Radiofrequency Power in Plasmas, May 14-17, 2019, Hefei, China, paper [accepted for publication in AIP Conf. Proceedings (2020)].

[44] W. Gekelman, P. Pribyl, Z. Lucky, M. Drandell, D. Leneman, J. Maggs, S. Vincena, B. Van Compernolle, S. K. P. Tripathi, G. Morales, T. A. Carter, Y. Wang, and T. DeHaas, Rev. Sci. Instrum. **87**, 025105 (2016).

[45] R.J. Perkins, J.C. Hosea , M.A. Jaworski , R.E. Bell , N. Bertelli , G.J. Kramer , L. Roquemore, G. Taylor and J.R. Wilson, Nuclear Materials and Energy **12**, 283 (2017).

[46] R. J. Perkins , J. C. Hosea, G. Taylor, N. Bertelli, G. J. Kramer, Z. P. Luo, C. M. Qin, L. Wang, J. C. Xu and X. J. Zhang, Plasma Phys. Control. Fusion **61**, 045011 (2019).

[47] V. Bobkov, R. Bilato, L. Colas, R. Dux, E. Faudot, H. Faugel, H. Fünfgelder, A. Herrmann, J. Jacquot, A. Kallenbach, et al., EPJ Web of Conferences **157**, 03005 (2017). DOI: 10.1051/epjconf/201715703005

[48] D.A. D'Ippolito, J.R. Myra, P.M. Ryan, E. Righi, J. Heikkinen, P.U. Lamalle, J.-M. Noterdaeme and Contributors to the EFDA–JETWorkprogramme, Nucl. Fusion **42**, 1356 (2002).

[49] E. Faudot, Phys. Plasmas **22**, 083506 (2015).

[50] M. J. Poulos, Phys. Plasmas **26**, 022104 (2019).

[51] G. Bal, B. Van Compernolle, M. Martin, W. Gekelman, P. Pribyl and T. A. Carter, 23rd Topical Conference on Radiofrequency Power in Plasmas, May 14-17, 2019, Hefei, China, paper P1.10 [AIP Conf. Proceedings (2020)].

[52] E. H. Martin, J. B. O. Caughman, C. C. Klepper, M. Goniche, R. C. Isler, J. Hillairet, and C. Bottereau, AIP Conference Proceedings 1689, 030011 (2015).

[53] A. Kostic, K. Crombé, M. Griener, R. Dux, M. Usoltceva, E. H. Martin, I. Shesterikov and J.-M. Noterdaeme, 23rd Topical Conference on Radiofrequency Power in Plasmas, May 14-17, 2019, Hefei, China, paper P1.12 [AIP Conf. Proceedings (2020)].

[54] K. Crombé, S. Devaux, R. D'Inca, E. Faudot, H. Faugel, H. Fünfgelder, S. Heuraux, J. Jacquot, F. Louche, J. Moritz, R. Ochoukov, M. Tripsky, D. Van Eester, T. Wauters, and J.-M. Noterdaeme, AIP Conference Proceedings **1689**, 030006 (2015).

[55] M. Usoltceva, W. Tierens, R. Ochoukov, A. Kostic, K. Crombé, S. Heuraux and J.-M. Noterdaeme, 23rd Topical Conference on Radiofrequency Power in Plasmas, May 14-17, 2019, Hefei, China, paper P1.14 [AIP Conf. Proceedings (2020)].

[56] S. Devaux, E. Faudot, J. Moritz, S. Heuraux, Nucl. Mater. Energy **12**, 908 (2017). https://doi.org/10.1016/j.nme.2017.07.003

[57] J. Ou, B. Lin, X. Zhao and Y. Yang, Plasma Phys. Control. Fusion **58**, 075004 (2016).

[58] S. Basnet, and R. Khanal, Phys. Plasmas **26**, 043516 (2019).

[59] J. Ou, X. An, and Z. Men, Phys. Plasmas **26**, 123514 (2019).

[60] D. A. D'Ippolito, J. R. Myra, J. Jacquinot and M. Bures, Phys. Fluids B **5**, 3603 (1993).

[61] M. Bécoulet, L. Colas, S. Pécoul, J. Gunn, Ph. Ghendrih, A. Bécoulet, S. Heuraux, Phys. Plasmas **9**, 2619 (2002).

[62] W. Zhang, Y. Feng, J.-M. Noterdaeme, V. Bobkov, L. Colas, D. Coster, T. Lunt, R. Bilato, J. Jacquot, R. Ochoukov, D. Van Eester, A. Křivská, P. Jacquet, L. Guimarais and the ASDEX Upgrade Team, Plasma Phys. Control. Fusion **58**, 095005 (2016).

[63] P. Tamain, C. Colin, L. Colas, C. Baudoin, G. Ciraolo, R. Futtersack, D. Galassi, Ph Ghendrih, N. Nace, F. Schwander, E. Serre, Nucl. Materials and Energy **12**, 1171 (2017).

[64] S. Sharma, A. Sen, N. Sirse, M. M. Turner, and A. R. Ellingboe, Phys. Plasmas **25**, 080705 (2018).

[65] M. M. Turner and P. Chabert, Appl. Phys. Lett. **104** , 164102 (2014).

[66] W. Gekelman, M. Barnes, S. Vincena, and P. Pribyl, Phys. Rev. Lett **103**, 045003 (2009).

[67] M. J. Martin, J. Bonde, W. Gekelman and P. Pribyl, Rev. Sci. Instrum. **86**, 053507 (2015).

[68] C. Lau, G. R. Hanson, B. Labombard, Y. Lin, O. Meneghini, R. Ochoukov, R. Parker, S. Shiraiwa, J. Terry, G. Wallace, J. Wilgen and S. J. Wukitch, Plasma Phys. Control. Fusion **55**, 025008 (2013).

[69] D. A. Schaffner, T. A Carter, G.D. Rossi, D. S. Guice, J. E. Maggs, S. Vincena, and B. Friedman, Phys. Rev. Lett **109**, 135002 (2012).

[70] M. J. Martin, "Radio Frequency Enhanced Plasma Potential and Flows in the Scrape-Off Layer of an Active Antenna," Section A2, Ph. D. thesis, UCLA, 2017. https://escholarship.org/uc/item/58t598ft

[71] J.R. Myra, C. Lau, B. Van Compernolle, S. Vincena and J. Wright, "Measurement and modeling of the radio frequency sheath impedance in a large magnetized plasma," Dataset, (Zenodo, 2020) http://doi.org/10.5281/zenodo.3746678